Ahmadpour, Najmeh; Sayadi, Mohammad Hossein; Homaeigohar, Shahin

A hierarchical Ca/TiO2/NH2-MIL-125 nanocomposite photocatalyst for solar visible light induced photodegradation of organic dye pollutants in water

Published in:
RSC Advances

DOI:
10.1039/d0ra05192f

Published: 12/08/2020

Document Version
Publisher's PDF, also known as Version of record

RSC Advances

ROYAL SOCIETY OF CHEMISTRY

PAPER

View Article Online
View Journal | View Issue

Cite this: *RSC Adv.*, 2020, **10**, 29808

A hierarchical Ca/TiO_2/NH_2-MIL-125 nanocomposite photocatalyst for solar visible light induced photodegradation of organic dye pollutants in water†

Najmeh Ahmadpour,[a] Mohammad Hossein Sayadi *[a] and Shahin Homaeigohar [bc]

In this study, for the first time, the Ca/TiO_2/NH_2-MIL-125 nanocomposite photocatalyst was synthesized for the purpose of photodegradation of Methyl Orange (MO) and Rhodamine B (RhB) dyes under visible light irradiation. The structural and chemical properties of the nanocomposite photocatalyst were characterized through FTIR, XRD, TGA, PL, XPS, ICP-OES and UV-DRS. For the photodegradation efficiency analysis, the effect of pH (3, 5, 7, 9, and 11), photocatalyst dosage (0.1, 0.2, 0.4, 0.6, and 0.8 g L^{-1}), dye concentration (1–40 mg L^{-1}), and contact time (10–120 min) was precisely evaluated. The largest photodegradation efficiency for RhB and MO dye models was 82.87% and 86.22%, respectively, that was obtained under optimal conditions in terms of pH and photocatalyst dosage and for Ca(30%)/TiO_2/NH_2-MIL-125. The photodegradation process of the dyes complied well with the first-order kinetic model. Moreover, the nanocomposite photocatalyst showed consistent photodegradation efficiency and after 6 successive cycles with fresh dye solutions, it could still perform comparably well. Taken together, Ca/TiO_2/NH_2-MIL-125 photocatalyst is able to show a high photodegradation efficiency for dye pollutants and optimum stability and reusability.

Received 12th June 2020
Accepted 27th July 2020

DOI: 10.1039/d0ra05192f

rsc.li/rsc-advances

1. Introduction

In recent decades, with the rapid development of industrial activities and with population growth, the discharge of highly toxic substances in water resources has dramatically increased.[1,2] The presence of organic matter, including dyes, in water streams, is undesirable even in small amounts and can prevent the penetration of light and oxygen into water and thereby decline the activity of photosynthetic and aquatic organisms.[3] Sewage from the textile industry contains a significant quantity of unstable dyes and mineral salts. To control the adverse impacts of the sewage disposal, degradation and removal of the existing chemical pollutants from wastewater is of utmost importance.[4] Dye compounds are often resistant to biodegradation due to their complex structure. These compounds are toxic, mutagenic and carcinogenic[5] and must be removed from waste water. Typically, dye is separated from industrial wastewater by coagulation, clotting, biological treatment,[6] chemical oxidation, electrochemical treatment,[7] ion exchange,[8] and surface adsorption.[9,10] Despite showing various merits, such methods are solely able to transform the dye molecules from one phase to another,[11] and do not entirely "eliminate" or "decompose" them. This deficiency could be challenging because disposal of the dye-derived sludge is problematic.[12] For such a reason, the degradation processes such as photocatalysis, *i.e.* advanced oxidation process (AOP) that allow decomposition of dye to nontoxic metabolites are preferred.[13]

Photocatalytic oxidation technology based on implementation of semiconductors has attracted a great deal of attention for environmental remediation due to the possibility of using solar energy as an abundant energy source, high conversion rate of solar energy, and high oxidation potential.[14] In recent years, TiO_2 nanoparticles have been considered as one of the most promising photocatalysts due to their high photocatalytic activity, stability, low cost and environmental compatibility.[15–17] Due to a high band gap energy (3.2 eV), this metal oxide is activated merely by ultraviolet (UV) irradiation. Thus, the photodegradation processes based on TiO_2 are not that versatile and economical. To address this concern, applicability of TiO_2 must be extended to solar visible light range, *e.g. via* doping that

[a]*Department of Environmental Engineering, Faculty of Natural Resources and Environment, University of Birjand, Birjand, Iran. E-mail: mh_sayadi@birjand.ac.ir; Fax: +98 5632254066; Tel: +98 5632254068*

[b]*School of Science & Engineering, University of Dundee, Dundee, DD1 4HN, UK*

[c]*Nanochemistry and Nanoengineering, Department of Chemistry and Materials Science, School of Chemical Engineering, Aalto University, Kemistintie 1, 00076 Aalto, Finland*

† Electronic supplementary information (ESI) available. See DOI: 10.1039/d0ra05192f

narrows the band gap, to assure cost and energy efficiency of the photocatalytic process. As another limitation, the recombination rate of electron–hole pairs created in TiO_2 is high and this renders it less attractive for photocatalytic processes due to a low quantum efficiency.[18] To overcome this deficiency, another catalyst should be coupled with TiO_2 to minimize recombination of electrons–hole pairs.[19]

In the last two decades, TiO_2 has been either doped with metal and non-metallic materials[20] and/or coupled with other semiconductors[21] to be active under sun light. Regarding the former approach, doping of TiO_2 with metal nanoparticles has drawbacks such as thermal instability and increased recombination rate of electron–hole pairs.[22] Whereas, coupling of TiO_2 with the semiconductors whose band gaps match that of it, is a more practical approach to create visible light driven TiO_2 photocatalysts. Additionally, this strategy is simple and the matched semiconductors are abundant.[23]

As a matched semiconductor for TiO_2, metal–organic frameworks (MOFs) have been frequently studied. MOFs comprising metal clusters interlinked with organic linkers, show a large surface area, high porosity and tunable pore size, thus can potentially be used for various advanced applications in energy, biomedicine, and water treatment.[24,25] These compounds contain electron-releasing groups and due to their appropriate optical response are considered suitable photocatalysts, that can be used in many relevant applications such as removal of organic pollutants.[26] For instance, MOF-5,[27] UiO-66(Zr), ZIF-8,[28] and MIL-125(Ti)[23] have served as semiconductor photocatalysts. However, such semiconductor MOFs are hardly operative for solar visible light photocatalysis, unless their organic linkers or metal clusters are properly modified.[29] As an example, NH_2-MIL-125(Ti) is the isostructural MOF of MIL-125(Ti) and comprises cyclic $Ti_8O_8(OH)_4$ oxoclusters and 2-aminoterephthalate ligands. Thanks to its amino functional groups, NH_2-MIL-125(Ti) shows an absorption spectra extending into the visible-light region (~550 nm).[30] Wang *et al.*[31] developed NH_2-MIL-125(Ti) as a multifunctional photocatalyst and validated that it can reduce Cr(VI) through its optimized photocatalytic activity under solar visible light.

As aforementioned, MOFs can be considered as matched semiconductors for TiO_2. This strategy has proven to be efficient for minimization of the chance of recombination of photogenerated electrons and holes. For instance, Zeng *et al.*[32] synthesized TiO_2/ZIF-8 nanofibers that were able to show an improved photodegradation efficiency for RhB as compared to TiO_2 or ZIF-8. Such an extraordinary photocatalytic activity was ascribed to the N–Ti–O chemical bond, developed by sonochemical treatment, between TiO_2 and ZIF-8 that possibly lowers recombination of the electron–hole pairs. The synergetic effect of MOF and TiO_2 in provision of an enhanced photocatalytic performance can be further supported by inclusion of metal nanoparticles as co-catalysts. In this regard, the photocatalytic activity of TiO_2/MOFs has been improved with incorporation of metal nanoparticles as seen for Pd/TiO_2/MIL-125(Ti)[33] and Cu/TiO_2/MOF[34] under visible light. While co-existence of noble metal co-catalysts and TiO_2 leads to formation of a Schottky junction on the interfacial surface, thereby facilitating charge-transfer,[33] alkaline earth metals can raise the number of surface reactive sites for adsorption and support charge separation,[35,36] thus increase the photodegradation efficiency. Among the alkaline earth metals, calcium is outstanding thanks to its excellent biocompatibility and environmentally friendliness, abundancy in the soil, and low cost. To the best of our knowledge, calcium has never been considered as a co-catalyst for TiO_2/MOFs. In this study, we aim to synthesize Ca/TiO_2/NH_2-MIL-125 nanocomposites and challenge their applicability with respect to photocatalytic degradation of MO and RhB dyes.

2. Materials and methods

2.1. Materials

Amino terephthalic acid (H_2ATA), dimethyl formamide (DMF), tetrabutyl titanate (TBT), calcium nitrate ($Ca(NO_3)_2$), hydrochloric acid (HCl), sodium hydroxide (NaOH), and methanol were purchased from Merck (Darmstadt, Germany). TiO_2 powder (Degussa; P25) was obtained from Degussa (Germany). Methyl orange and rhodamine B dyes were purchased from Sigma Aldrich (US). All the chemicals were of analytical grade and used without purification.

2.2. Preparation of TiO_2/NH_2-MIL-125

NH_2-MIL-125 was synthesized through a modified solvothermal method.[30] In this method, amino terephthalic acid (H_2ATA) (0.5 g, 3 mmol) as a linker and TBT (0.26 mL, 0.75 mmol) were added to DMF (9 mL)–methanol (1 mL) mixture solvent. The as-made solution was stirred at room temperature for 30 minutes, then transferred into a 50 mL Teflon liner and heated at 150 °C for 72 hours. The suspension formed after the hydrothermal treatment was cooled down to room temperature and then filtered. The filtrate was washed twice with DMF, to remove the unreacted organic ligands, and then washed several times with methanol to exchange DMF with methanol. Finally, the obtained yellowish powder was dried in the vacuum oven for 6 hours at 60 °C. For preparation of TiO_2/NH_2-MIL-125, the same entire procedure was followed, except that 0.3 mg of P25 powder was added to the mixture solution of NH_2-MIL-125 and stirred for 30 minutes. Eventually, the resulting mixture was washed several times with DMF and methanol and was dried at 60 °C for 4 hours under vacuum.[23]

2.3. Preparation Ca/TiO_2/NH_2-MIL-125

Ca/TiO_2/NH_2-MIL-125 photocatalyst was prepared through a solvothermal process. For this purpose, TiO_2/NH_2-MIL-125 was dissolved in $Ca(NO_3)_2 \cdot 4H_2O$ at room temperature and stirred for 20 min to end up with a homogenous solution. To prepare Ca/TiO_2/NH_2-MIL-125 nanocomposite with different Ca concentrations of 5, 10, 20, 30, and 40%, different weight percentages of the calcium precursor were used. The resulting solution was then transferred to a 100 mL reaction vessel, wherein it was heated for 2 days at 90 °C. The formed crystals were washed with DMF and then centrifuged and dried to obtain Ca/TiO_2/NH_2-MIL-125 with different percentages of Ca.[37]

2.4. Characterization of Ca/TiO_2/NH_2-MIL-125 nanocomposite

The crystalline structure of the nanocomposite photocatalyst was characterized by X-ray diffraction (Rigaku MiniFlex 600, Japan) using Cu-Kα radiation (λ = 0.15418 nm). X-ray Photoelectron Spectroscopy (XPS) (Thermo Scientific K-Alpha X-ray Photoelectron Spectrometer, USA) and Fourier Transform Infrared Spectroscopy (FTIR) (Shimadzu, FTIR1650 spectrophotometer, Japan) were also applied to determine the chemical features of the nanocomposite photocatalyst. The UV-Vis spectra of the specimens were measured by a UV-Vis spectrophotometer (Shimadzu, UV-2550, Japan). Thermogravimetry analysis (TGA) was done using a Perkin Elmer device (USA) with a heating rate of 10 °C min^{-1} under nitrogen atmosphere. The amount of Ca in the nanocomposite samples was determined by inductively coupled plasma-optical emission spectrometry (ICP-OES, Leeman Direct Reading Echelle). The photoluminescence (PL) spectra were measured by using an excitation wavelength of 300 nm in an Agilent instrument (model G9800A). Zeta potential measurements were performed to assess zeta potential and isoelectric point of the nanoparticles using a Zetasizer (3000HS) machine. The mineralization degree was determined *via* total organic carbon (TOC) measurements by using an Analytik Jena device (Germany).

2.5. Photodegradation test

Batch photodegradation experiments were performed in a 1000 mL reactor containing 50 mL of dye solution (20 mg L^{-1}) and 50 mg photocatalyst at room temperature. In each experiment, a certain amount of the photocatalyst (0.1, 0.2, 0.4, 0.6 and 0.8 g L^{-1}) was added to the reactor and the whole assembly was irradiated with the simulated visible light by a 300 W Xe-lamp. 50 mg of photocatalyst Ca/TiO_2/NH_2-MIL-125 was added to 50 mL of MO and RhB dyes solutions with an initial concentration of 20 mg L^{-1}, stirred in dark condition for 30 min to obtain adsorption–desorption equilibrium.

The effect of pH on the photodegradation efficiency of the photocatalyst was also probed. For this sake, pH values (3, 5, 7, 9 and 11) of the dye solutions were adjusted by addition of HCl (0.1 M) and NaOH (0.1 M) and controlled using a pH meter (Istek, 915PDC, Korea). Over a 120 min time period, after each 30 min, 5 mL of the dye solution was taken and centrifuged immediately and the dye concentration was determined by a spectrophotometer (at the characteristic wavelength of 464 nm and 554 nm for MO and for RhB, respectively). The absorption intensity was correlated to dye concentration through a previously established calibration curve. The photodegradation efficiency of MO and RhB was calculated *via* the eqn (1):

$$\text{Photodegradation efficiency } (\%) = \frac{C_0 - C_t}{C_0} \times 100 \qquad (1)$$

where C_0 and C_t are the initial and momentary concentration of dye, respectively.

2.6. Photocatalytic nanoparticle shelf life analysis

To characterize the shelf life of the nanocomposite photocatalyst, the most optimum composition, as determined through the photodegradation tests, *i.e.* Ca(30%)/TiO_2/NH_2-MIL-125 (0.2 g L^{-1}) was suspended in 20 mL deionized water and sonicated for 15 minutes. The resulting suspension was kept for 1, 2, 4, 6, 9 and 12 months at 30 °C. During this period, the suspension was stirred periodically. Finally, the Ca(30%)/TiO_2/NH_2-MIL-125 photocatalyst was separated through centrifugation and washed 3 times with methanol to remove residual water. The photocatalyst was eventually dried under vacuum for 24 hours and used for further analysis.

3. Results and discussion

3.1. XRD analysis

XRD was used to determine the crystalline structure of the nanocomposite photocatalyst. Fig. 1a shows the XRD patterns of the various photocatalysts synthesized in this study. In this figure, the peaks appearing at 30.27°, 35.21°, 47.76°, 53.83° and 57.7° are correlated to the TiO_2 anatase crystalline planes of (220), (311), (200), (422) and (511), respectively (according to JCPDS 21-1272).[38] The peaks present at 5.7°, 7.5°, and 10° are attributed to (200), (210) and (220) crystalline planes of NH_2-MIL-125, respectively.[39] Co-existence of the peaks relevant to TiO_2 and NH_2-MIL-125, in the spectra of TiO_2/NH_2-MIL-125 implies successful synthesis of this nanocomposite photocatalyst. After inclusion of Ca, however, no new distinct peak emerges, probably due to the low concentration of the Ca added. This finding has been previously reported by other researchers, as well.[40,41]

3.2. FTIR analysis

To investigate the surface chemistry of Ca(5, 10, 20, 30, and 40%)/TiO_2/NH_2-MIL-125 photocatalysts, FTIR analysis was performed. As shown in Fig. 1b, the peaks seen at 1384, 1235, 1660, and 1680 cm^{-1} correspond to the carboxylic acid group, CN group,[42] symmetrical and asymmetrical groups of carboxylic acid,[43] and NH group[23] of NH_2-MIL-125, respectively. TiO_2/NH_2-MIL-125 showed extra peaks at 450, 1410, and 3418 cm^{-1} attributed to stretching vibrations of Ti–O,[44] carboxylic group, and OH group,[45] respectively. As can be seen, inclusion of calcium does not lead to any significant change in the position of the peaks of TiO_2/NH_2-MIL-125, implying no particular destruction of NH_2-MIL-125 structure.

3.3. Thermal stability analysis (TGA)

Thermal stability of Ca(5, 10, 20, 30, and 40%)/TiO_2/NH_2-MIL-125 photocatalysts, was characterized through TGA analysis. As shown in Fig. 1c, in the case of control (TiO_2) sample, weight loss after the entire heating cycle was only 3.84%, most likely due to residual alcohol or water evaporation. With respect to the other samples, weight declined in three stages: (1) between 50 and 150 °C due to evaporation of residual water; (2) between 150 and 300 °C, due to the exclusion of organic ligands present in the reaction,[46] and (3) between 300 and 500 °C due to thermal degradation of NH_2-MIL-125. NH_2-MIL-125 alone shows an optimum thermal stability,[23] that is further promoted by inclusion of TiO_2 and Ca. This behavior can be ascribed to the fact that the thermal breakdown of ligands, including DMF and H_2ATA, is reduced.[26]

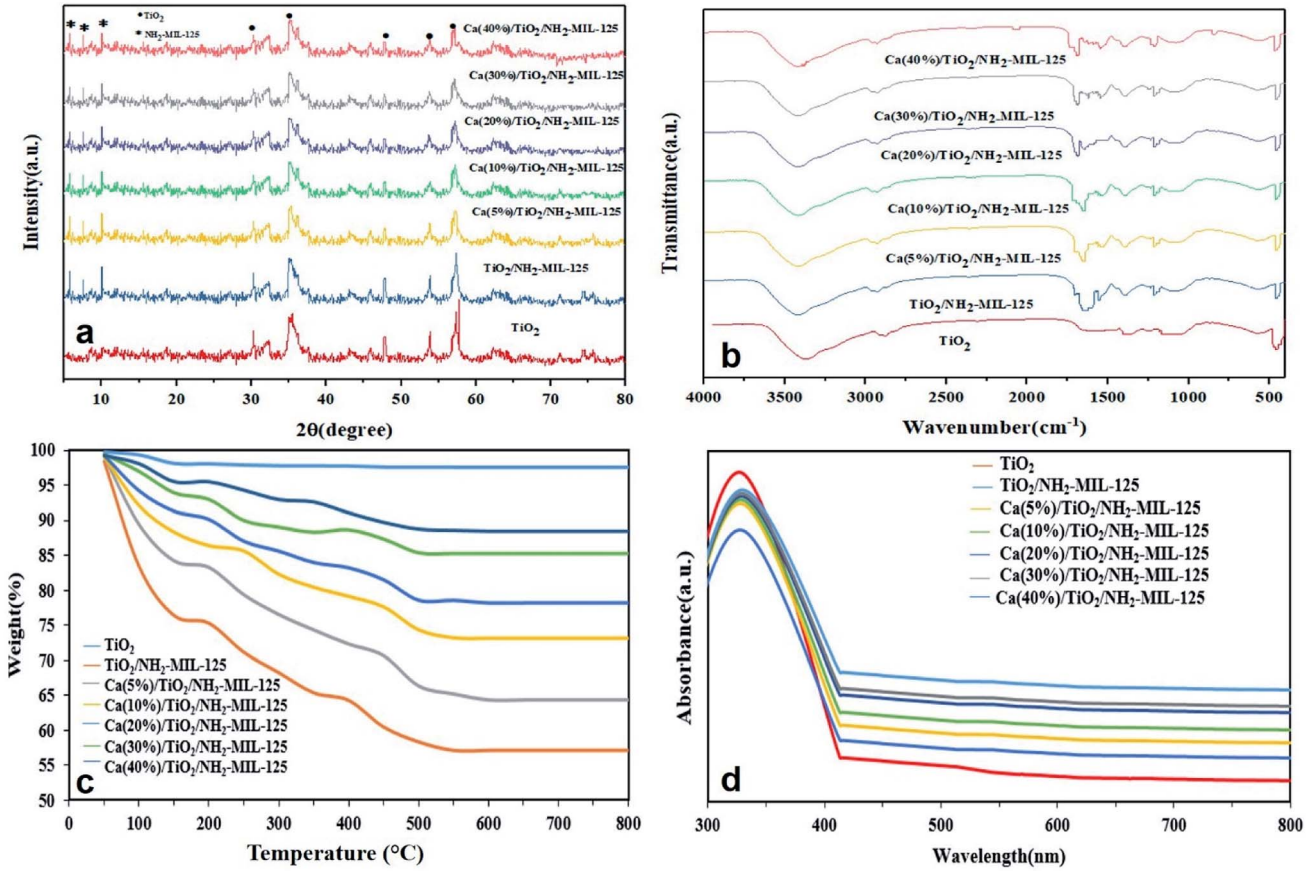

Fig. 1 (a) XRD, (b) FTIR, (c) TGA and (d) UV-Vis DR spectra of the Ca/TiO_2/NH_2-MIL-125 nanocomposite photocatalysts (note that TiO_2 and TiO_2/NH_2-MIL-125 were considered as the controls).

3.4. UV-Vis diffuse reflectance spectra (DRS) analysis

As can be seen in Fig. 1d, the Ca(5, 10, 20, 30, and 40%)/TiO_2/NH_2-MIL-125 photocatalysts show an almost identical UV light absorption intensity, originated from the presence of TiO_2 anatase phase.[33] Among these compositions, the UV light absorption intensity rises proportional to Ca content and the respective peaks also red shift. The former observation might stem from the formation of the Schottky junctions between TiO_2 and Ca, which facilitate the charge transfer. Also, plasmon resonance levels, arisen from the mass oscillation of conduction band electrons, and their interaction with electromagnetic radiation could play a role in the enhanced absorption of UV light. However, the plasmonic band of Ca in the solar light region was not observed due to the tiny size of the particles and the low calcium content.[45] Therefore, the enhanced light absorption capacity of the nanocomposite photocatalysts potentially leads to an increased photocatalytic efficiency and thereby a higher photodegradation rate of organic pollutants.

3.5. XPS analysis

The surface chemistry of the Ca/TiO_2/NH_2-MIL-125 nanocomposite photocatalyst was probed through XPS analysis. Fig. 2a shows the general XPS spectrum of the sample, implying the presence of O, Ti, N, C, and Ca. As shown in Fig. 2b, the connection energy of $Ti2p_{1/2}$ and $Ti2p_{3/2}$ is represented in the peaks appearing at 458.5 and 464.5 eV, respectively, assigned to Ti4 mode in the Ti–O band.[44] The O1s spectra are shown in Fig. 2c, wherein the peaks emerged at 530.4, 529.4, and 529.9 can be assigned to carboxyl group, oxy titanium cluster, and OH species, respectively.[33,47,48] According to C1s spectra, Fig. 2d, the peaks appearing at 284.8 eV, 284.5 eV, 288 eV, and 285.2 eV are assigned to CN, CC, C=O, and C=C, respectively.[48] In Fig. 2e, demonstrating the N1s spectra, the peaks at 399.5 eV and 401.6 eV represent the amine group of NH_2-M125 to –NH_2 (–NH– and –N=).[31] Lastly, Fig. 2f shows the Ca2p spectra with the peaks at 350.6 and 347 eV that are attributed to $Ca^2p_{1/2}$ and $Ca^2p_{3/2}$.[36]

3.6. Photoluminescence analysis

Photoluminescence (PL) spectroscopy was performed to characterize the electron transfer behavior of the nanocomposite photocatalyst and its ability in separation of light-generated charge carriers. Fig. 3a shows that a sharp peak appears at 466 nm, that is attributed to the intensive PL emission of TiO_2, due to the high recombination rate of electrons–hole pairs. Compared to TiO_2, the fluorescence intensity of TiO_2/NH_2-MIL-125 and Ca/TiO_2/NH_2-MIL-125 decreases dramatically, implying the enhanced carrier separation efficiency of these

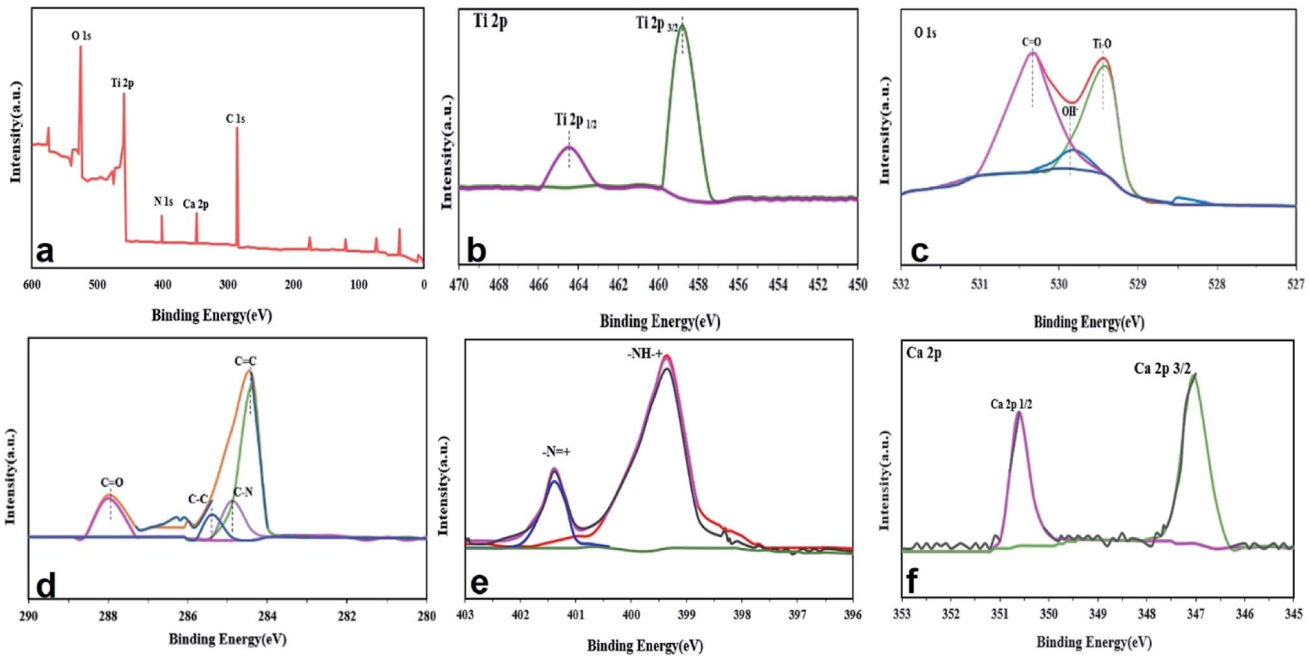

Fig. 2 XPS analysis of Ca/TiO_2/NH_2-MIL-125 photocatalyst: (a) general XPS spectrum of the compound, and (b) Ti2p, (c) O1s, (d) C1s, (e) N1s and (f) Ca2p spectra.

photocatalysts. Among the Ca doped photocatalysts, the lowest PL intensity belongs to Ca(30%)/TiO_2/NH_2-MIL-125, witnessing its lowest recombination rate of electrons–hole pairs. It also shows the most efficient separation of electrons–hole pairs and the longest carrier length. In fact, with the larger addition of Ca, the number of trapping sites for the light-emitting electrons declines and thus a lower PL peak intensity is arisen.

3.7. Photodegradation efficiency of the nanocomposite photocatalysts

Photocatalytic degradation of MO and RhB dye models by the synthesized nanocomposite photocatalysts was thoroughly investigated. In order to maintain a balance in the absorption–desorption performance of the photocatalyst, the dye solution was first kept in dark for 30 minutes. Afterwards, the photodegradation experiments, taking into account parameters such as the photocatalyst dosage of 0.2 g L^{-1}, the dye concentration of 5 mg L^{-1} and pH 7 were carried out. As shown in Fig. 3b and c, the highest photodegradation efficiencies were recorded as much as 87.29% and 83.12% for MO and RhB, respectively. The best photodegradation performance belonged to Ca(30%)/TiO_2/NH_2-MIL-125, due to the least recombination rate of electrons–hole pairs.

The highest dye photodegradation efficiency was achieved by Ca(30%)/TiO_2/NH_2-MIL-125 catalyst, thanks to a reduced recombination rate of electrons–hole pairs. Accordingly, this particular photocatalyst was based for the next measurements. Among the studied photocatalysts, TiO_2 and TiO_2/NH_2-MIL-125

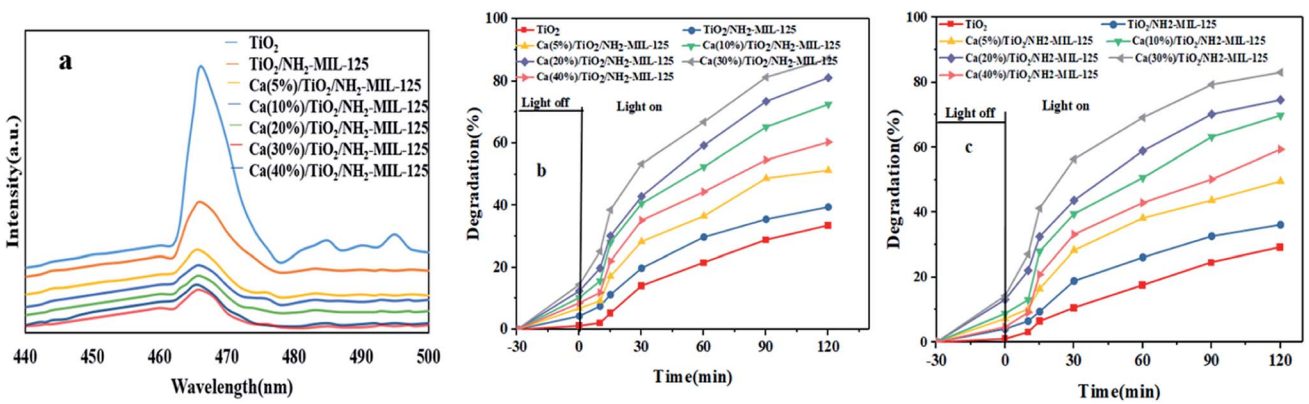

Fig. 3 (a) Photoluminescence (PL) analysis of Ca/TiO_2/NH_2-MIL-125 photocatalyst, visible light induced photodegradation efficiency of Ca/TiO_2/NH_2-MIL-125 photocatalyst over a 120 min time period for MO (b) and RhB (c).

showed the lowest photodegradation efficiency. Upon inclusion of Ca, the photodegradation efficiency increased significantly. The NH_2-MIL-125 phase facilitates the dye removal through dye adsorption as well as increased light absorption. Mahmoodi *et al.* also believe that Ca transmits plasmon energy and helps the charge transfer between TiO_2 and NH_2-MIL-125(Ti) (NMT) phases, thereby increasing photocatalytic degradation. Such a synergistic photodegradation effect has been previously reported for a photocatalyst composed of Ag/AgCl@$CoFe_2O_4$/NH_2-MIL-125(Ti) (CFNMT). This nanocomposite photocatalyst is able to remove 93% RhB which is superior to that of Ag/AgCl, NMT, and CFNMT alone.[49]

3.8. The effect of pH

The dye photodegradation efficiency of Ca(30%)/TiO_2/NH_2-MIL-125 photocatalyst was evaluated under different pH values of 3, 5, 7, 9, and 11. As mentioned earlier, in these measurements, the photocatalyst dosage of 0.2 g L^{-1} and MO and RhB dye concentration of 5 mg L^{-1} were taken into account.

As shown in Fig. 4a and b, the highest and lowest dye photodegradation efficiency are observed at pH 5 and pH 11, respectively. After 120 minutes visible light irradiation, the dye degradation efficiency was 68.35% (pH 3), 83.21% (pH 5), 53.25% (pH 7), 34.87% (pH 9) and 31.2% (pH 11) for MO and 70.87% (pH 3), 81.36% (pH 5), 56.85% (pH 7), 38.74% (pH 9) and 30.12% (pH 11) for RhB. As can be observed, in general lower pH values are more effective in MO and RhB dyes removal efficiency. Protonation of the surface of the photocatalyst at acidic pH values facilitates electrostatic interaction with anionic dye models and raises their adsorption and later their photodegradation. Surprisingly, pH 5 provides better photodegradation conditions than pH 3 does, most likely due to an excessive density of protons at pH 3 that potentially inactivate hydroxide ions and thereby lower the number of active radicals after light irradiation.

The isoelectric point of the photocatalyst is 4.6, thus at pH values below pH_{pzc}, the surface is highly protonated and thus positively charged. In contrast, at pH values over 4.6, due to the extensive presence of OH^- ions, the surface is negatively charged, Fig. 4c. Considering the negative charge and anionic nature of the dye models, protonation of the functional groups of the photocatalyst at low pH values is favorable for electrostatic interaction between the dye molecules and the photocatalyst surface. Moreover, abundance of H^+ ions in an acidic medium brings about large formation of hydroxyl radicals, thereby engendering high photodegradation extent of organic pollutants.[42] In contrast, in an alkaline medium, the negatively charged sites are abundant. This feature leads to electrostatic repulsion of the dye molecules and poor dye degradation. Furthermore, the amount of insoluble compounds formed during the reaction rises. This consequence reduces the transmitted light intensity and thereby hampers formation of hydroxyl radicals and lowers the photodegradation efficiency.

3.9. The effect of photocatalyst dosage

In this part, the effect of photocatalyst dosage (0.1, 0.2, 0.4, 0.6 and 0.8 g L^{-1}) on photodegradation extent of MO and RhB dye models was investigated. As shown in Fig. 5a, up to a certain limit, the larger the photocatalyst dosage, the higher the photodegradation efficiency is. This limit for MO and RhB dye models is 0.4 and 0.2 g L^{-1}, respectively. At such dosages, the number of reactive sites increases proportional to the density of the photocatalyst particles and thereby the interaction of the dye molecules and their adsorption level as well as the number of the produced OH reactive radicals rise. Afterwards, the photodegradation efficiency declines with the photocatalyst dosage, most likely due to large aggregation of the photocatalyst particles that renders their surface less exposed to the dye solution and also reduces the intensity of the transmitted light into the solution.[50,51]

3.10. Effect of initial dye concentration

The effect of initial dye concentration on photocatalytic degradation of MO and RhB by Ca(30%)/TiO_2/NH_2-MIL-125 was determined. For this purpose, optimal photocatalyst dosages of 0.4 g L^{-1} for MO and 0.2 g L^{-1} for RhB and optimum pH of 5 were considered. As shown

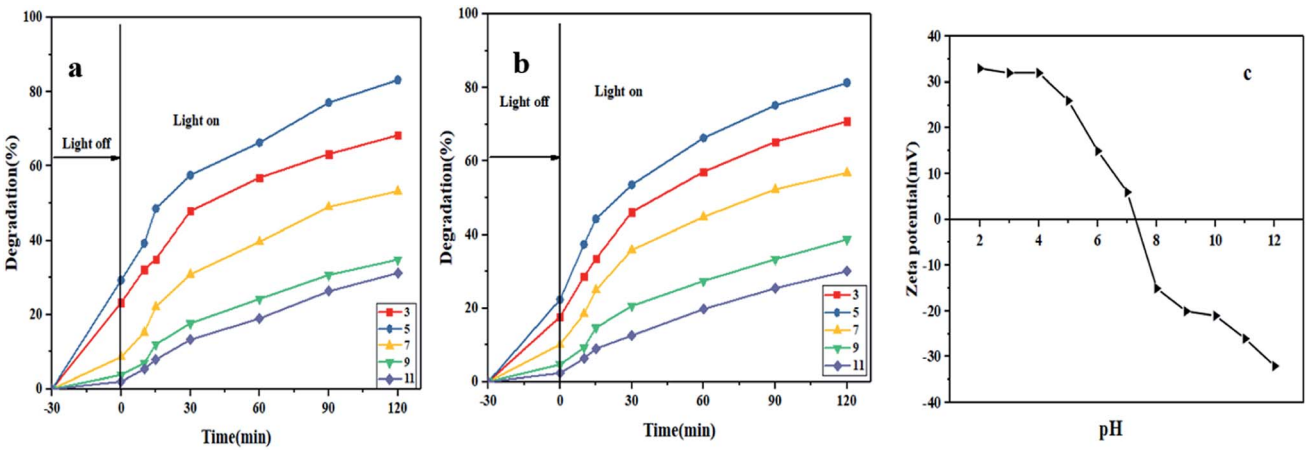

Fig. 4 The effect of pH on photocatalytic degradation of MO (a) and RhB (b) by Ca(30%)/TiO_2/NH_2-MIL-125 (dye concentration: 5 mg L^{-1}, photocatalyst dosage: 0.2 g L^{-1}, visible light irradiation); (c) zeta potential measurement at different pHs.

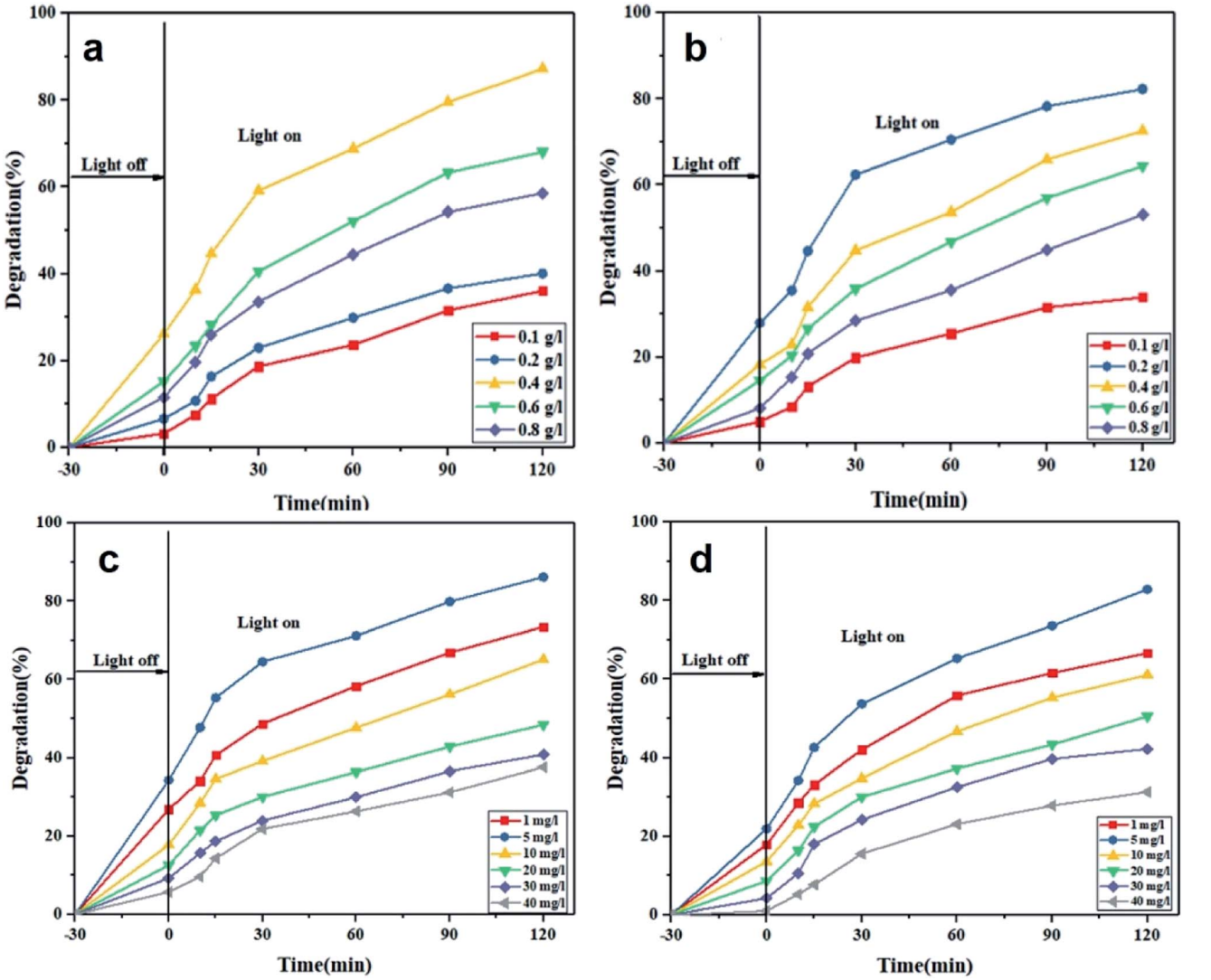

Fig. 5 Effect of photocatalyst dosage on photocatalytic degradation of MO (a) and RhB (b) (dye concentration: 5 mg L^{-1}, pH = 5, visible light irradiation). Effect of initial dye concentration on photocatalytic degradation of MO (c) and RhB (d) (pH = 5, photocatalyst dosage: 0.4 g L^{-1} for MO and 0.2 g L^{-1} for RhB, visible light irradiation).

in Fig. 5c and d, the photodegradation efficiency decreases with increasing the initial dye concentration. The highest and lowest dye removal took place for 5 and 40 mg L^{-1} initial dye concentrations, regardless of the dye type. Also, with increasing the contact time between the dye molecules and the photocatalyst, the removal efficiency is promoted. This feature is ascribed to the increased density of the cavities and thereby larger production of H^+ and OH^- ions over time.[52] The greater photodegradation efficiency at low initial dye concentrations is justified by the larger density of hydroxyl radicals and more effective excitation of the photocatalyst nanoparticles under visible light irradiation.[53] However, at a fixed photocatalyst dosage, when the initial dye concentration rises, an insufficient density of hydroxyl radicals is available that cannot effectively degrade the dye molecules. Therefore, photodegradation efficiency at high initial dye concentrations drops. Another reason for this loss in photodegradation efficiency is the light absorption by the dye molecules that prevent the transfer of photons to the photocatalyst surface.[54]

3.11. Photodegradation kinetics

The kinetics of the photodegradation reactions was determined to further comprehend the involved mechanisms. Similar to many other relevant studies, the first-order kinetic model was used to uncover the mechanism of photocatalytic degradation of the dye models. In this regard, the Langmuir–Hinshelwood (L–H) model was employed to explain the photodegradation mechanism of MO and RhB dyes under the most optimum conditions (eqn (2) and (3)):

$$C = C_0\, e^{-k_{app} t} \quad (2)$$

$$\ln\left(\frac{C}{C_0}\right) = -k_{app} t \quad (3)$$

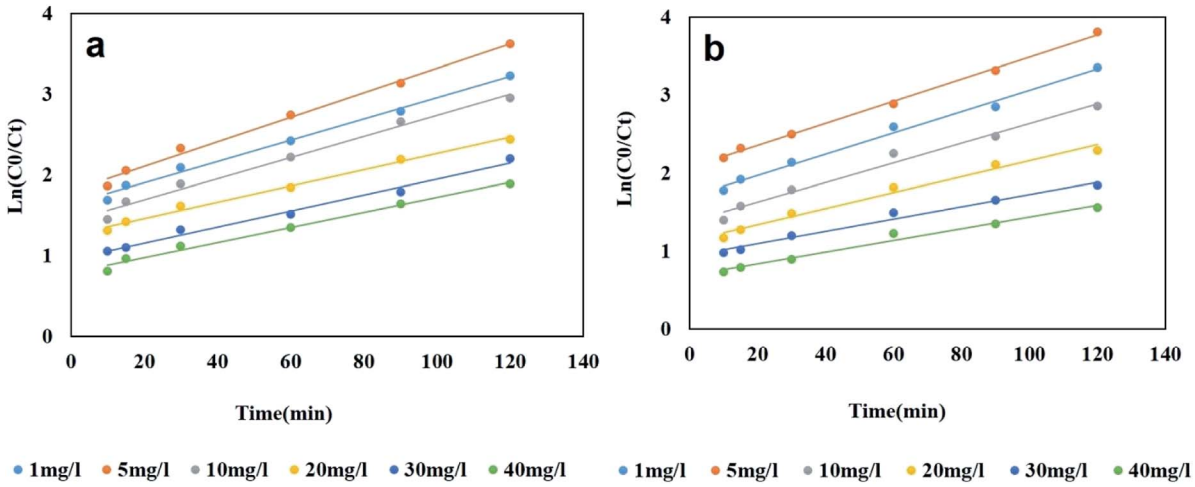

Fig. 6 Kinetic plots of photodegradation process of MO (a) and RhB (b) (dye concentrations: 1–40 mg L^{-1}, pH 5, photocatalyst dosage: 0.4 g L^{-1} for MO and 0.2 g L^{-1} for RhB).

where C and C_0 are the momentary and initial dye concentrations, respectively. k and t are the reaction rate and time constants, respectively.[55]

Fig. 6a and b imply the linearity of the $\ln(C_0/C_t)$ curves *versus* time, as well as their high correlation coefficient, respectively. As can be seen in ESI Table SM1,† k declines with increasing the

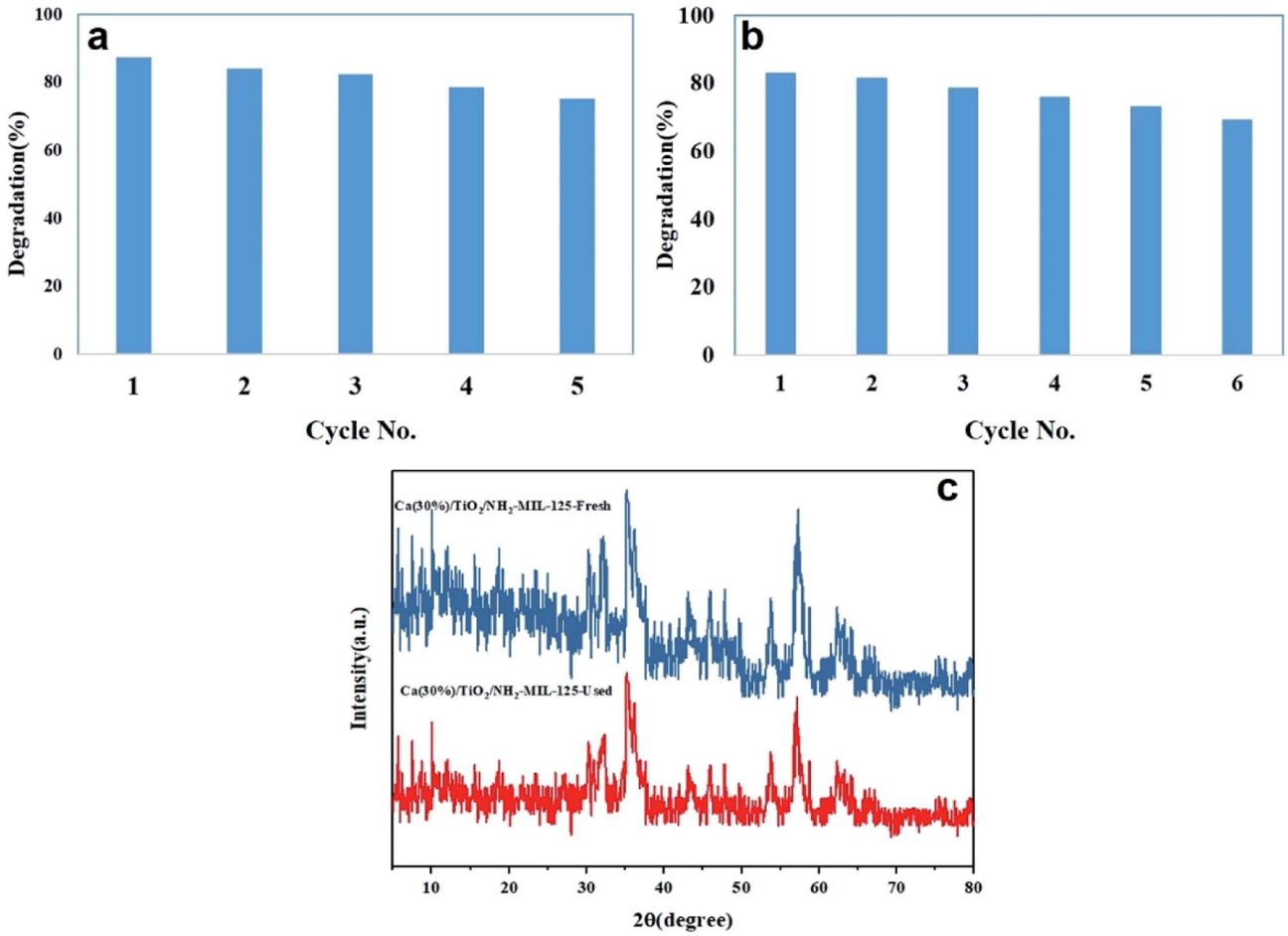

Fig. 7 Reusability of Ca(30%)/TiO_2/NH_2-MIL-125 photocatalyst after 6 cycles of photodegradation of MO (a) and RhB (b). (c) XRD pattern of the photocatalyst before and after 6 cycles photodegradation.

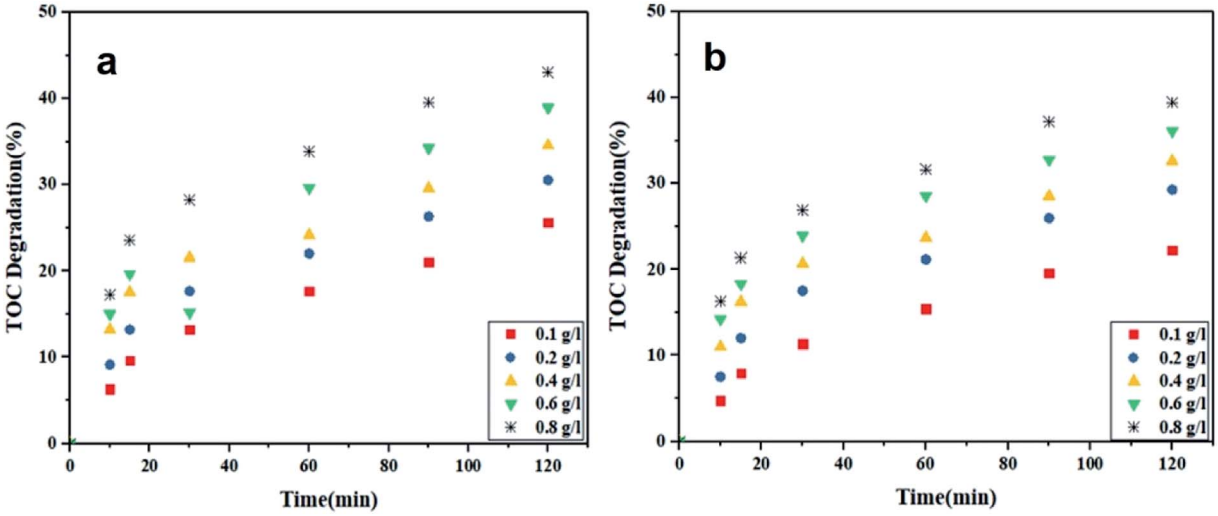

Fig. 8 TOC degradation in the MO (a) and RhB (b) dye solutions by Ca(30%)/TiO_2/NH_2-MIL-125 in different concentrations (dye concentration: 5 mg L^{-1} and pH = 5).

dye concentration, most likely due to formation of intermediate products that lower the amount of hydroxyl radicals, thereby negatively impacting the photodegradation efficiency at larger dye concentrations.[56]

3.12. Reusability and stability

Reusability and stability of a photocatalyst are among the most important factors influencing its practical applications. To probe how reusable and stable the photocatalyst is, after each photodegradation cycle, it was collected, washed with water and methanol and eventually dried at 90 °C for 24 hours under vacuum. The as-recycled photocatalyst was used for new photodegradation tests under optimal conditions. As shown in Fig. 7a and b, the photodegradation efficiency in the first cycle was 86.22% (MO) and 82.87% (RhB), and after 6 cycles it drops to 73.29% (MO) and 69.18% (RhB). Such an insignificant loss in photodegradation efficiency indicates the promising reusability of this photocatalyst. Interestingly, the ICP-OES analysis of the nanoparticles showed that only 2% Ca is lost during the whole process, implying the excellent stability of the nanocomposite photocatalyst. This fact was further verified by XRD test. As shown in Fig. 7c, after 6 cycles of reuse, no obvious structural change can be traced in the photocatalyst.

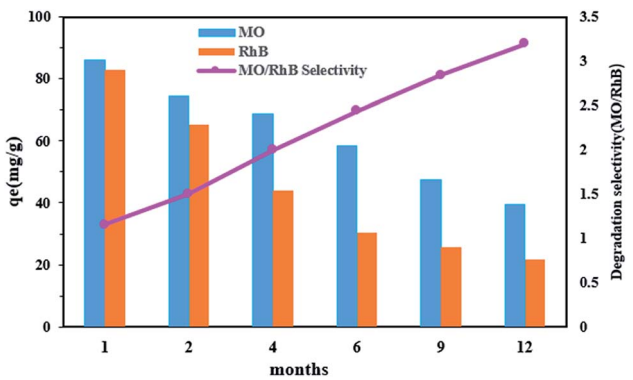

Fig. 9 Effect of water aging on MO and RhB photodegradation efficiency by Ca(30%)/TiO_2/NH_2-MIL-125.

3.13. Total organic carbon (TOC) analysis

TOC analysis was performed to evaluate the TOC removal through the photodegradation process using Ca(30%)/TiO_2/NH_2-MIL-125. As shown in Fig. 8a and b, the TOC removal percentage was 43.02% for MO and 39.47% for RhB containing solutions, while the photodegradation efficiency for these dyes was notably higher. Such a discrepancy stems from the presence of mediators (byproducts) formed during the photocatalytic process.[57]

3.14. The water aging of photocatalytic nanoparticles

The aging time of the nanocomposite photocatalyst (Ca(30%)/TiO_2/NH_2-MIL-125) might alter through time dependent microstructural change and affect the dye photodegradation efficiency. To assess the shelf life of Ca(30%)/TiO_2/NH_2-MIL-125, variation of photodegradation efficiency of the photocatalyst over a time period of one year at intervals of 1, 2, 4, 6, 9, and 12 months was monitored. As shown in Fig. 9, as long as the photocatalyst is aged, its dye photodegradation efficiency declines. The ideal photodegradation selectivity for MO over RhB by the photocatalyst was obtained using the isotherm, eqn (4):[58]

$$S = \frac{q_{MO}/C_{MO}}{q_{RhB}/C_{RhB}} \quad (4)$$

where S is the ideal selection indicator for photodegradation, q_{MO} and q_{RhB} are the MO and RhB equilibrium adsorption efficiency, respectively. C is MO and RhB concentration. According to Fig. 9, with increasing the aging time of the photocatalytic nanoparticles, their photodegradation selectivity for

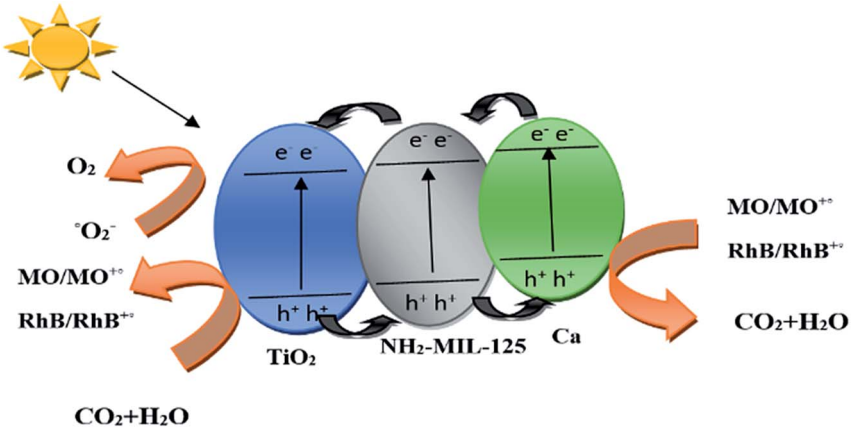

Fig. 10 Mechanism of photodegradation process of MO and RhB by Ca(30%)/TiO_2/NH_2-MIL-125 photocatalyst.

MO rises. This issue could be related to increment of the zeta potential with aging time (Table SM2†), and bond dissociation between the metal cluster and the ligand,[59] that leads to exposure of carboxyl groups. As a result, the electrostatic interaction between the anionic color (MO) and the positively charged nanoparticles increases.

3.15. Photodegradation mechanism

As shown in Fig. 10, under visible light radiation, electrons in the TiO_2 valence band (VB) are stimulated and jump to the conduction band (CB), leading to the production of electrons and holes. Due to the high conductivity of calcium, such electrons are transferred from the TiO_2 CB to the calcium surface and react with the oxygen at the TiO_2 surface, thereby generating radical O_2. At the same time, the electrons in the TiO_2 (CB) and the charge carrier generated are transferred to NH_2-MIL-125 and thereby reduce the recombination rate of electron–hole pairs. In addition, the holes in the TiO_2 (CB) can oxidize water and improve the photocatalytic efficiency. In general, $^{\bullet}O_2$ and $^{\bullet}OH$ radicals and holes are the main charge carriers and oxidizing agents in the photodegradation process of the organic dye pollutants. In our system, the synergistic effect between NH_2-MIL-125 and Ca significantly improves the photocatalytic function of TiO_2 and enables it to photodegrade MO and RhB dyes more efficiently. The main photodegradation reactions are as follow:

$$Ca/TiO_2/NH_2\text{-MIL-125} \xrightarrow{\text{UV light}} h^+ + e^- \quad (5)$$

$$e^- + O_2 \rightarrow {}^{\bullet}O_2^- \quad (6)$$

$${}^{\bullet}O_2^- + \text{pollutant} \rightarrow CO_2 + H_2O \quad (7)$$

$$h^+ + \text{pollutant} \rightarrow CO_2 + H_2O \quad (8)$$

$$h^+ + H_2O \rightarrow {}^{\bullet}OH + H \quad (9)$$

$${}^{\bullet}OH + \text{pollutant} \rightarrow CO_2 + H_2O \quad (10)$$

4. Conclusion

We successfully synthesized highly reactive and stable nanocomposite photocatalysts composed of Ca/TiO_2/NH_2-MIL-125 *via* a solvothermal treatment and used them for photodegradation of MO and RhB dye models. The results showed that Ca(30%)/TiO_2/NH_2-MIL-125 was the most efficient photocatalyst with the largest photodegradation efficiency under visible light irradiation. This superior photocatalytic activity could be attributed to the narrow band gap of the photocatalyst and the synergistic effect of the constituting materials. In terms of kinetics, the photocatalytic reactions complied well with the first-order kinetic model. Interestingly, the photodegradation efficiency of the photocatalyst did not decline notably after 6 times reuse, implying its promising stability and reusability. Taken together, the developed nanocomposite photocatalyst is robust and persistent in terms of photodegradation performance, and can remove hazardous dye pollutants from water in an environmentally friendly manner.

Conflicts of interest

There are no conflicts to declare.

Acknowledgements

N. A. and M. H. S. gratefully acknowledge the Research Council of University of Birjand (Grant Number: 2948/1399) for the financial support. Also they appreciate the assistance of laboratories in the Faculty of Natural Resources and Environment, University of Birjand, during the course of the experiments and analysis.

References

1 C. Saucier, M. A. Adebayo, E. C. Lima, R. Cataluna, P. S. Thue, L. D. Prola, M. Puchana-Rosero, F. M. Machado, F. A. Pavan and G. Dotto, Microwave-assisted activated carbon from cocoa shell as adsorbent for removal of sodium diclofenac

and nimesulide from aqueous effluents, *J. Hazard. Mater.*, 2015, **289**, 18–27.

2 M. Ghadimi, S. Zangenehtabar and S. Homaeigohar, An Overview of the Water Remediation Potential of Nanomaterials and Their Ecotoxicological Impacts, *Water*, 2020, **12**(4), 1150.

3 N. M. Mahmoodi, Photodegradation of dyes using multiwalled carbon nanotube and ferrous ion, *J. Environ. Eng.*, 2013, **139**(11), 1368–1374.

4 M. Mon, R. Bruno, J. Ferrando-Soria, D. Armentano and E. Pardo, Metal–organic framework technologies for water remediation: towards a sustainable ecosystem, *J. Mater. Chem. A*, 2018, **6**(12), 4912–4947.

5 G. Ramesha, A. V. Kumara, H. Muralidhara and S. Sampath, Graphene and graphene oxide as effective adsorbents toward anionic and cationic dyes, *J. Colloid Interface Sci.*, 2011, **361**(1), 270–277.

6 G. Ersan, O. G. Apul, F. Perreault and T. Karanfil, Adsorption of organic contaminants by graphene nanosheets: a review, *Water Res.*, 2017, **126**, 385–398.

7 V. Markou, M.-C. Kontogianni, Z. Frontistis, A. G. Tekerlekopoulou, A. Katsaounis and D. Vayenas, Electrochemical treatment of biologically pre-treated dairy wastewater using dimensionally stable anodes, *J. Environ. Manage.*, 2017, **202**, 217–224.

8 M. A. Chamjangali, G. Bagherian, A. Javid, S. Boroumand and N. Farzaneh, Synthesis of Ag–ZnO with multiple rods (multipods) morphology and its application in the simultaneous photo-catalytic degradation of methyl orange and methylene blue, *Spectrochim. Acta, Part A*, 2015, **150**, 230–237.

9 A. H. Abdullah, E. A. Abdullah, Z. Zainal, M. Z. Hussein and T. K. Ban, Adsorptive performance of penta-bismuth hepta-oxide nitrate, Bi5O7NO3, for removal of methyl orange dye, *Water Sci. Technol.*, 2012, **65**(9), 1632–1638.

10 S. Homaeigohar, The Nanosized Dye Adsorbents for Water Treatment, *Nanomaterials*, 2020, **10**(2), 295.

11 X. Liu, Z. Xing, Y. Zhang, Z. Li, X. Wu, S. Tan, X. Yu, Q. Zhu and W. Zhou, Fabrication of 3D flower-like black N-TiO2-x@MoS2 for unprecedented-high visible-light-driven photocatalytic performance, *Appl. Catal., B*, 2017, **201**, 119–127.

12 P. Bansal, G. R. Chaudhary and S. K. Mehta, Comparative study of catalytic activity of ZrO2 nanoparticles for sonocatalytic and photocatalytic degradation of cationic and anionic dyes, *Chem. Eng. J.*, 2015, **280**, 475–485.

13 O. Mekasuwandumrong, P. Pawinrat, P. Praserthdam and J. Panpranot, Effects of synthesis conditions and annealing post-treatment on the photocatalytic activities of ZnO nanoparticles in the degradation of methylene blue dye, *Chem. Eng. J.*, 2010, **164**(1), 77–84.

14 Y. Deng and R. Zhao, Advanced oxidation processes (AOPs) in wastewater treatment, *Curr. Pollut. Rep.*, 2015, **1**(3), 167–176.

15 N. Ahmadpour, M. H. Sayadi, A. Verma and B. Mansouri, Ultrasonic degradation of ibuprofen from the aqueous solution in the presence of titanium dioxide nanoparticles/hydrogen peroxide, *Desalin. Water Treat.*, 2019, **145**, 291–299.

16 S. Homaeigohar, N. K. Botcha, E. S. Zarie and M. Elbahri, Ups and Downs of Water Photodecolorization by Nanocomposite Polymer Nanofibers, *Nanomaterials*, 2019, **9**(2), 250.

17 S. Sh. Homaeigohar, H. Mahdavi and M. Elbahri, Extraordinarily water permeable sol gel formed nanocomposite nanofibrous membranes, *J. Colloid Interface Sci.*, 2012, **366**, 51–56.

18 W. Fan, C. Chen, H. Bai, B. Luo, H. Shen and W. Shi, Photosensitive polymer and semiconductors bridged by Au plasmon for photoelectrochemical water splitting, *Appl. Catal., B*, 2016, **195**, 9–15.

19 H. Zabihi-Mobarakeh and A. Nezamzadeh-Ejhieh, Application of supported TiO2 onto Iranian clinoptilolite nanoparticles in the photodegradation of mixture of aniline and 2,4-dinitroaniline aqueous solution, *J. Ind. Eng. Chem.*, 2015, **26**, 315–321.

20 M. Janus, J. Zatorska, A. Czyżewski, K. Bubacz, E. Kusiak-Nejman and A. W. Morawski, Self-cleaning properties of cement plates loaded with N, C-modified TiO2 photocatalysts, *Appl. Surf. Sci.*, 2015, **330**, 200–206.

21 H. Tada, T. Mitsui, T. Kiyonaga, T. Akita and K. Tanaka, All-solid-state Z-scheme in CdS–Au–TiO 2 three-component nanojunction system, *Nat. Mater.*, 2006, **5**(10), 782–786.

22 J. Schneider, M. Matsuoka, M. Takeuchi, J. Zhang, Y. Horiuchi, M. Anpo and D. W. Bahnemann, Understanding TiO_2 photocatalysis: mechanisms and materials, *Chem. Rev.*, 2014, **114**(19), 9919–9986.

23 X. Zhao, Y. Zhang, P. Wen, G. Xu, D. Ma and P. Qiu, NH2-MIL-125(Ti)/TiO2 composites as superior visible-light photocatalysts for selective oxidation of cyclohexane, *Mol. Catal.*, 2018, **452**, 175–183.

24 C. Lu, T. Ben, S. Xu and S. Qiu, Electrochemical Synthesis of a Microporous Conductive Polymer Based on a Metal–Organic Framework Thin Film, *Angew. Chem., Int. Ed.*, 2014, **53**(25), 6454–6458.

25 M.-H. Zeng, Z. Yin, Y.-X. Tan, W.-X. Zhang, Y.-P. He and M. Kurmoo, Nanoporous Cobalt(II) MOF Exhibiting Four Magnetic Ground States and Changes in Gas Sorption upon Post-Synthetic Modification, *J. Am. Chem. Soc.*, 2014, **136**(12), 4680–4688.

26 X. Xu, R. Liu, Y. Cui, X. Liang, C. Lei, S. Meng, Y. Ma, Z. Lei and Z. Yang, PANI/FeUiO-66 nanohybrids with enhanced visible-light promoted photocatalytic activity for the selectively aerobic oxidation of aromatic alcohols, *Appl. Catal., B*, 2017, **210**, 484–494.

27 B. Civalleri, F. Napoli, Y. Noël, C. Roetti and R. Dovesi, *Ab initio* prediction of materials properties with CRYSTAL: MOF-5 as a case study, *CrystEngComm*, 2006, **8**(5), 364–371.

28 J. H. Choi, Y. J. Choi, J. W. Lee, W. H. Shin and J. K. Kang, Tunability of electronic band gaps from semiconducting to metallic states *via* tailoring Zn ions in MOFs with Co ions, *Phys. Chem. Chem. Phys.*, 2009, **11**(4), 628–631.

29 H. Khajavi, J. Gascon, J. M. Schins, L. D. A. Siebbeles and F. Kapteijn, Unraveling the Optoelectronic and

Photochemical Behavior of Zn4O-Based Metal Organic Frameworks, *J. Phys. Chem. C*, 2011, **115**(25), 12487–12493.

30 Y. Fu, D. Sun, Y. Chen, R. Huang, Z. Ding, X. Fu and Z. Li, An Amine-Functionalized Titanium Metal–Organic Framework Photocatalyst with Visible-Light-Induced Activity for CO2 Reduction, *Angew. Chem., Int. Ed.*, 2012, **51**(14), 3364–3367.

31 H. Wang, X. Yuan, Y. Wu, G. Zeng, X. Chen, L. Leng, Z. Wu, L. Jiang and H. Li, Facile synthesis of amino-functionalized titanium metal-organic frameworks and their superior visible-light photocatalytic activity for Cr (VI) reduction, *J. Hazard. Mater.*, 2015, **286**, 187–194.

32 X. Zeng, L. Huang, C. Wang, J. Wang, J. Li and X. Luo, Sonocrystallization of ZIF-8 on Electrostatic Spinning TiO2 Nanofibers Surface with Enhanced Photocatalysis Property through Synergistic Effect, *ACS Appl. Mater. Interfaces*, 2016, **8**(31), 20274–20282.

33 B. Yan, L. Zhang, Z. Tang, M. Al-Mamun, H. Zhao and X. Su, Palladium-decorated hierarchical titania constructed from the metal-organic frameworks NH2-MIL-125(Ti) as a robust photocatalyst for hydrogen evolution, *Appl. Catal., B*, 2017, **218**, 743–750.

34 R. Li, S. Wu, X. Wan, H. Xu and Y. Xiong, Cu/TiO 2 octahedral-shell photocatalysts derived from metal–organic framework@ semiconductor hybrid structures, *Inorg. Chem. Front.*, 2016, **3**(1), 104–110.

35 N. I. Al-Salim, S. A. Bagshaw, A. Bittar, T. Kemmitt, A. James McQuillan, A. M. Mills and M. J. Ryan, Characterisation and activity of sol–gel-prepared TiO photocatalysts modified with Ca, Sr or Ba ion additives, *J. Mater. Chem.*, 2000, **10**(10), 2358–2363.

36 W. Fu, S. Ding, Y. Wang, L. Wu, D. Zhang, Z. Pan, R. Wang, Z. Zhang and S. Qiu, F, Ca co-doped TiO 2 nanocrystals with enhanced photocatalytic activity, *Dalton Trans.*, 2014, **43**(43), 16160–16163.

37 J. Liao, B. Jin, Y. Zhao and Z. Liang, Highly efficient and durable metal-organic framework material derived Ca-based solid sorbents for CO2 capture, *Chem. Eng. J.*, 2019, **372**, 1028–1037.

38 J. Zhang, Y. Hu, J. Qin, Z. Yang and M. Fu, TiO2-UiO-66-NH2 nanocomposites as efficient photocatalysts for the oxidation of VOCs, *Chem. Eng. J.*, 2020, **385**, 123814.

39 B. J. Smith, A. C. Overholts, N. Hwang and W. R. Dichtel, Insight into the crystallization of amorphous imine-linked polymer networks to 2D covalent organic frameworks, *Chem. Commun.*, 2016, **52**(18), 3690–3693.

40 W. Cui, J. Shang, H. Bai, J. Hu, D. Xu, J. Ding, W. Fan and W. Shi, In-situ implantation of plasmonic Ag into metal-organic frameworks for constructing efficient Ag/NH2-MIL-125/TiO2 photoanode, *Chem. Eng. J.*, 2020, **388**, 124206.

41 V. Ramasubbu, P. R. Kumar, E. M. Mothi, K. Karuppasamy, H.-S. Kim, T. Maiyalagan and X. S. Shajan, Highly interconnected porous TiO2-Ni-MOF composite aerogel photoanodes for high power conversion efficiency in quasi-solid dye-sensitized solar cells, *Appl. Surf. Sci.*, 2019, **496**, 143646.

42 R. Liang, L. Shen, F. Jing, W. Wu, N. Qin, R. Lin and L. Wu, NH2-mediated indium metal–organic framework as a novel visible-light-driven photocatalyst for reduction of the aqueous Cr (VI), *Appl. Catal., B*, 2015, **162**, 245–251.

43 Z. Yang, X. Xu, X. Liang, C. Lei, Y. Wei, P. He, B. Lv, H. Ma and Z. Lei, MIL-53 (Fe)-graphene nanocomposites: efficient visible-light photocatalysts for the selective oxidation of alcohols, *Appl. Catal., B*, 2016, **198**, 112–123.

44 R. Zhang, M. Shao, S. Xu, F. Ning, L. Zhou and M. Wei, Photo-assisted synthesis of zinc-iron layered double hydroxides/TiO2 nanoarrays toward highly-efficient photoelectrochemical water splitting, *Nano Energy*, 2017, **33**, 21–28.

45 H. Song, Z. Sun, Y. Xu, Y. Han, J. Xu, J. Wu, T. Sun, H. Meng and X. Zhang, Fabrication of NH2-MIL-125(Ti) incorporated TiO2 nanotube arrays composite anodes for highly efficient PEC water splitting, *Sep. Purif. Technol.*, 2019, **228**, 115764.

46 M. H. Sayadi, S. Sobhani and M. Hajiani, A potential natural solar light active photocatalyst using magnetic $ZnFe_2O_4$@TiO_2/Cu nanocomposite as a high performance and recyclable platform for degradation of naproxen from aqueous solution, *J. Clean. Prod.*, 2020, **268**, 122023.

47 C. Zhang, L. Ai and J. Jiang, Graphene hybridized photoactive iron terephthalate with enhanced photocatalytic activity for the degradation of rhodamine B under visible light, *Ind. Eng. Chem. Res.*, 2015, **54**(1), 153–163.

48 J.-M. Wu, Y. Chen, L. Pan, P. Wang, Y. Cui, D. Kong, L. Wang, X. Zhang and J.-J. Zou, Multi-layer monoclinic BiVO4 with oxygen vacancies and V4+ species for highly efficient visible-light photoelectrochemical applications, *Appl. Catal., B*, 2018, **221**, 187–195.

49 N. M. Mahmoodi, A. Taghizadeh, M. Taghizadeh and J. Abdi, In situ deposition of Ag/AgCl on the surface of magnetic metal-organic framework nanocomposite and its application for the visible-light photocatalytic degradation of Rhodamine dye, *J. Hazard. Mater.*, 2019, **378**, 120741.

50 N. Ahmadpour, M. H. Sayadi, S. Sobhani and M. Hajiani, Photocatalytic degradation of model pharmaceutical pollutant by novel magnetic TiO_2@ $ZnFe_2O_4$/Pd nanocomposite with enhanced photocatalytic activity and stability under solar light irradiation, *J. Environ. Manage.*, 2020, **271**, 110964.

51 X. Hou, S. L. Stanley, M. Zhao, J. Zhang, H. Zhou, Y. Cai, F. Huang and Q. Wei, MOF-based C-doped coupled TiO_2/ZnO nanofibrous membrane with crossed network connection for enhanced photocatalytic activity, *J. Alloys Compd.*, 2019, **777**, 982–990.

52 A. Yazdani and M. H. Sayadi, Sonochemical degradation of azithromycin in aqueous solution, *Environ. Health Eng. Manage. J.*, 2018, **5**(2), 85–92.

53 E. Bazrafshan, S. Noorzaei and F. KordMostafapour, Photocatalytic degradation of aniline in aqueous solutions using magnesium oxide nanoparticles, *J. Mazandaran Univ. Med. Sci.*, 2016, **26**(139), 126–136.

54 M. N. Chong, S. Lei, B. Jin, C. Saint and C. W. Chow, Optimisation of an annular photoreactor process for degradation of Congo Red using a newly synthesized

titania impregnated kaolinite nano-photocatalyst, *Sep. Purif. Technol.*, 2009, **67**(3), 355–363.

55 E. S. Elmolla and M. Chaudhuri, Degradation of amoxicillin, ampicillin and cloxacillin antibiotics in aqueous solution by the UV/ZnO photocatalytic process, *J. Hazard. Mater.*, 2010, **173**(1), 445–449.

56 L. Yang, L. Xu, X. Bai and P. Jin, Enhanced visible-light activation of persulfate by Ti3+ self-doped TiO2/graphene nanocomposite for the rapid and efficient degradation of micropollutants in water, *J. Hazard. Mater.*, 2019, **365**, 107–117.

57 M. H. Sayadi, S. Sobhani and H. Shekari, Photocatalytic degradation of azithromycin using GO@Fe3O4/ZnO/SnO2 nanocomposites, *J. Clean. Prod.*, 2019, **232**, 127–136.

58 H. Molavi, A. Hakimian, A. Shojaei and M. Raeiszadeh, Selective dye adsorption by highly water stable metal-organic framework: long term stability analysis in aqueous media, *Appl. Surf. Sci.*, 2018, **445**, 424–436.

59 J. B. DeCoste, G. W. Peterson, H. Jasuja, T. G. Glover, Y.-g. Huang and K. S. Walton, Stability and degradation mechanisms of metal–organic frameworks containing the Zr6O4(OH)4 secondary building unit, *J. Mater. Chem. A*, 2013, **1**(18), 5642–5650.

